

An Operational Radiometric Landsat Preprocessing Framework for Large-Area Time Series Applications

David Frantz, Achim Röder, Marion Stellmes, and Joachim Hill

Abstract—We developed a large-area preprocessing framework for multisensor Landsat data, capable of processing large data volumes. Cloud and cloud shadow detection is performed by a modified Fmask code. Surface reflectance is inferred from Tanré's formulation of the radiative transfer, including adjacency effect correction. A precompiled MODIS water vapor database provides daily or climatological fallback estimates. Aerosol optical depth (AOD) is estimated over dark objects (DOs) that are identified in a combined database and image-based approach, where information on their temporal persistency is utilized. AOD is inferred with consideration of the actual target reflectance and background contamination effect. In case of absent DOs in bright scenes, a fallback approach with a modeled AOD climatology is used instead. Topographic normalization is performed by a modified C-correction. The data are projected into a single coordinate system and are organized in a gridded data structure for simplified pixel-based access. We based the assessment of the produced data set on an exhaustive analysis of overlapping pixels: 98.8% of the redundant overlaps are in the range of the expected $\pm 2.5\%$ overall radiometric algorithm accuracy. AOD is in very good agreement with Aerosol Robotic Network sunphotometer data (R^2 : 0.72 to 0.79, low intercepts, and slopes near unity). The uncertainty in using the water vapor fallback climatology is approximately $\pm 2.8\%$ for the TM SWIR1 band in the wet season. The topographic correction was considered successful by an investigation of the nonrelationship between the illumination angle and the corrected radiance.

Index Terms—Atmospheric correction, cloud detection, Landsat, large area, multitemporal, southern Africa, surface reflectance, topographic correction.

I. INTRODUCTION

LANDSAT data are one of the most valuable resources for Earth observation [1] due to their long-term data continuity [2] and their optimal resolution to monitor processes at the landscape level [3]. With the advent of open data policy [4], accompanied by technical progress in terms of processing,

storing, and transmission infrastructure and the increasing availability of automated processing routines (e.g., [5]), the usage of Landsat data changed fundamentally [6]. Historically, analyses were either based on a few images and large areas [7] or on small areas and shorter time steps [8]. Now, it has become feasible to make use of the full depth of the Landsat archive, as well as covering very large areas at the same time. Nevertheless, Landsat data are still provided in the traditional Worldwide Reference System 2 (WRS-2) framework [9], where the image footprints vary from acquisition to acquisition. This involves several obstacles for the end user, e.g., the integrated usage of data from different paths requires the reprojection to a unique coordinate system, which simplifies the adequate usage of the data-rich orbital overlap area. Even in the case of using only one WRS-2 footprint, all images have to be cropped to the same extent. This is even mandatory if sophisticated follow-up applications such as time series analyses (TSA) or the derivation of pixel-based composites (PBC) [10] are to be addressed. The usage of these dense time series applications requires the data of a given location to be easily and quickly accessible, regardless of their initial path and row designation, projection, acquisition time, or sensor. Therefore, preprocessed imagery in a gridded data structure represents a more suitable structure for TSA or PBC applications [9], as demonstrated by the Web-enabled Landsat Data project [11].

Existing large-area production systems [9] or similar preprocessing architectures [11] most often do not include a full and integrated radiometric treatment, i.e., accounting for atmospheric and topographic effects simultaneously. Topographic variation even has a greater impact on the remotely sensed data than atmospheric effects [12]; thus, topography should be accounted for if the area of interest is not merely flat. More sophisticated analyses of large amounts of data such as spectral unmixing or the quantitative derivation of biomass indicators (e.g., in support for monitoring systems in a Reducing Emissions from Deforestation and forest Degradation (REDD) in developing countries context) for several or many time steps also require more sophisticated radiometric corrections, i.e., surface reflectance products. Reference [9] has recently published an overview of several Landsat data processing systems for large-area monitoring, whereby the corrections range from top-of-atmosphere (TOA) reflectance to surface reflectance, some of them including topographic and/or directional effects. Most systems only correct the data to TOA reflectance [9]. The widely used Landsat Ecosystem Disturbance Adaptive Processing System (LEDAPS) [13] produces surface reflectance by

Manuscript received May 4, 2015; revised October 17, 2015 and February 9, 2016; accepted February 11, 2016. Date of publication March 7, 2016; date of current version May 24, 2016. This work was funded by the Federal Ministry of Education and Research under Contract FKZ-01LG1201C as part of the Southern African Science Service Centre for Climate Change and Adaptive Land Management project.

This paper has supplementary downloadable material available at <http://ieeexplore.ieee.org>, provided by the authors.

The authors are with Trier University, 54296 Trier, Germany (e-mail: frantz@uni-trier.de; roeder@uni-trier.de; stellmes@uni-trier.de; hillj@uni-trier.de).

Color versions of one or more of the figures in this paper are available online at <http://ieeexplore.ieee.org>.

Digital Object Identifier 10.1109/TGRS.2016.2530856

utilizing radiative transfer modeling, although the system does not account for topography. Of note is the Eastern Australia preprocessing framework [14] that minimizes atmospheric, topographic, and bidirectional effects, although their integrated BRDF correction might not allow the direct transfer to areas that suffer from low data availability.

Large-area generation systems that apply a terrain normalization and provide gridded surface reflectance products of multisensor Landsat data are still scarce or require input data that may not be available in each part of the world. As such, we chose a sufficiently elaborate method set that minimizes the amount of input data, in order to provide a processing framework that may even be applied in areas where the general data availability is still low and where specific environmental settings preclude the usage of specific processing strategies, e.g., in our study area in southern Africa. We here present an operational approach that processes all available multisensor Level 1T (L1T) Landsat digital number (DN) data to surface reflectance and stores the processed data in a gridded tile structure as known from the MODIS land products. The generated products are tailored for applications that require rapid and easy data access, make use of a large amount of data across space and time, and demand radiometrically normalized data. The processing scheme includes modules for cloud masking, atmospheric and topographic correction, reprojection, and gridding.

II. STUDY AREA

The method was developed in southern Africa, entirely including the countries of Angola, Zambia, Zimbabwe, Botswana, and Namibia (ca. 3.7 Mio. km²). The area was designated because nationwide and cross-national wall-to-wall mapping of forest and ecosystem related parameters are to be targeted in the future, thus the inclusion of whole countries. For example, any REDD+ assessment should monitor deforestation and forest degradation rates at the national level to avoid leakage to unobserved spots [15]. In addition, the countries themselves were chosen because their national territory partially falls into the Kavango–Zambezi Transfrontier Conservation Area (KAZA TFCA), which is planned to be centered on the Caprivi–Chobe–Victoria Falls area. Thus, the area is a highly interesting spot for any kind of cross-boundary studies regarding a wide variety of ecological and social questions. The area is climatically diverse, particularly owing to the latitudinal precipitation gradient, mainly as a consequence of the Intertropical Convergence Zone [16]. The vegetation cover ranges from dense Miombo forests in Angola to sparse xerilic savanna ecosystems in the Kalahari and includes more extreme surface types such as swamps, salt pans, and deserts [17]. The seasonal cycle is closely tied to seasonal changes in large-scale air movement and solar configuration, which results in three hygrothermal seasons that spatially and annually differ in timing and length due to the variability in precipitation [18]: 1) hot wet season (~November to April); 2) cool dry season (~May to August); and 3) hot dry season (~September to October). The study area is presented in Fig. 1. Nonetheless, the presented preprocessing scheme is not bound to this area and can be ported elsewhere.

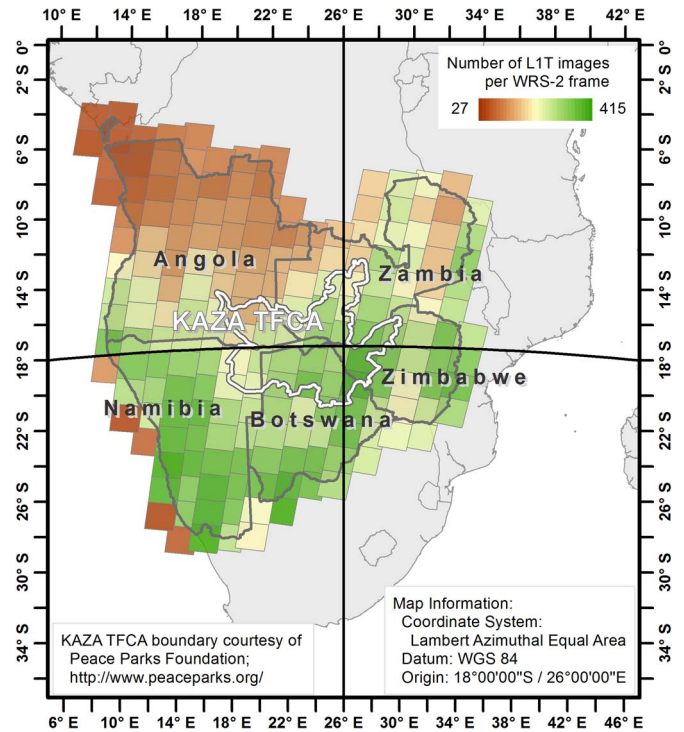


Fig. 1. Location of the study area and number of available L1T images per Landsat frame.

TABLE I
ACQUIRED L1T LANDSAT IMAGES

	Number	Size	Start	End
<i>L4 TM</i>	225	0.03	10/22/1987	03/27/1993
<i>L5 TM</i>	24,204	3.34	04/12/1984	11/17/2011
<i>L7 ETM+ SLC-On</i>	7,166	1.83	06/30/1999	05/28/2003
<i>L7 ETM+ SLC-Off</i>	20,816	4.44	07/22/2003	12/31/2014
<i>L8 OLI</i>	6,332	5.53	04/11/2013	12/31/2014

Number, compressed data volume in TB and time range of the acquired images.

III. DATA

A. Landsat Data

All available intersecting Landsat images from 194 WRS-2 frames were acquired from the U.S. Geological Survey (USGS) archive. We downloaded even very cloudy images of up to 70% cloud coverage because the Automated Cloud Cover Assessment system occasionally fails to estimate the cloud coverage with sufficient precision [5]. We discarded images that were not corrected with the Level 1 Product Generation System (LPGS) to L1T precision, as a reliable coregistration among images was considered to be of major importance for TSA and PBC follow-up applications. At the time of writing, we acquired and processed 58 731 L1T images, with a total data volume of nearly 15 TB (see Table I for details).

Fig. 1 displays the total number of available images for each WRS-2 frame. The data availability is quite low when compared with other areas such as the United States. There is a pronounced north–south gradient, where data availability is extremely low in northern Angola due to the characteristic regional rainfall patterns where the northwestern part of the study area is already located in the tropics. Fig. 2 displays all

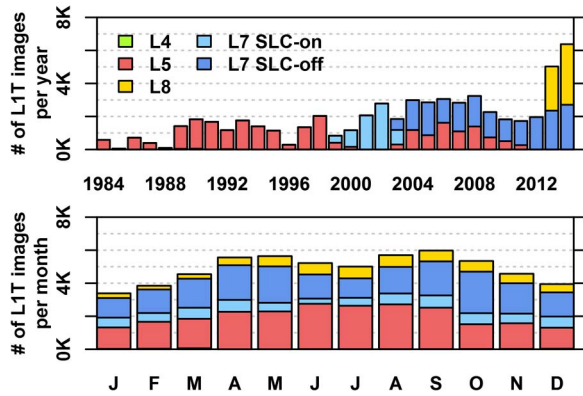


Fig. 2. Number of available L1T images per (top) year and (bottom) month.

available Landsat images for each year (top) and each month (bottom). The data availability is unevenly distributed among the years, e.g., due to satellite (de-) commissioning, changes in acquisition strategies, technical failure, climatic reasons, and so forth. There is a seasonality in data availability, with more data during the dry season and less data during the wet season. The Landsat Global Archive Consolidation effort [19] is currently still in progress, and we might expect up to 200 additional Landsat images per frame [20], which will significantly foster the applicability of subsequent analyses approaches—provided that each image is of sufficient quality to be processed to L1T precision.

B. DEM

Recently, USGS publicly released the 1-arc-second (~ 30 m) digital elevation model (DEM) derived by the Shuttle Radar Topography Mission (SRTM) [21]. We precompiled an elevation mosaic generously covering all of subequatorial Africa. DEM data are used for the topographic correction and for applying an elevation correction to the optical depths.

C. Precipitable Water Vapor

MODIS water vapor data are used for the physically based correction of water vapor absorption in the Earth's atmosphere. We use the MOD05 and MYD05 products, as well as the MOD03 and MYD03 geolocation tables, which are automatically downloaded from the Level 1 and Atmosphere Archive and Distribution System at NASA Goddard Space Flight Center. We use data that were derived from the near-infrared (NIR) water vapor algorithm [22], which relies on water vapor attenuation of the NIR radiation. The column water vapor amount is determined from radiative transfer theory on basis of ratios between water vapor absorbing and atmospheric window bands. The product is obtained at 1-km spatial resolution, and the temporal resolution is up to one day if considering both Aqua and Terra observations.

IV. METHODS

The presented framework for processing Landsat data from L1 DN values to a gridded surface reflectance product is

schematically shown in Fig. 3. The download of Landsat and SRTM data, as well as the mosaicking of the DEM, is performed rather manually in advance. The core functionality of the framework is enclosed in the solid box, where the main modules are the identification of clouds and cloud shadows (B), the radiometric processing (C), and geometric modules for the finishing of the data (D). The radiometric correction combines methods for atmospheric (C.2) and topographic corrections (C.3), which rely on the computation of the angular scene parameters, the derivation of topographic information, and an elaborated scheme for retrieving aerosol optical depth (AOD) in a joint database-, image- and object-based approach (C.2-b). The gaseous transmission is accounted for by a MODIS-derived water vapor database, which is scheduled operationally (C.2-a). Table II defines the mathematical symbols used in this paper.

A. Implementation

The code is able to process Landsat images from the Thematic Mapper (TM), Enhanced Thematic Mapper (ETM+), and Operational Land Imager (OLI) sensors. For the sake of data set consistency, we opted for processing only the traditional six reflective bands. Thus, we omit the ultra blue and cirrus bands of the OLI sensor. We also do not make use of the Landsat-8 quality layer for the same reason as that of not using the cirrus band in Fmask, as opposed to [23].

Detailed processing information of the key modules is appended to the metadata in order to enable the user to gauge the quality of the processed images.

The framework is entirely implemented with open source software and is written in C. The Geospatial Data Abstraction Library [24] API is used for reading data in GeoTiff and hierarchical data format (HDF) format, as well as for reprojection purposes. The cURL API is used for the automatic download of MODIS data. The GNU Scientific Library is used for optimization procedures. On-node and across-node parallelization are achieved by using GNU parallel [25], where one processor is fed with one image at a time. The processing chain is streamlined in random access memory such that the data are only read once and only the very final output is written to disk.

Several modules can be disabled or enabled in any possible combination, e.g., the topographic correction, reprojection, and/or tiling modules. The atmospheric correction can be also switched off, in which case TOA reflectance is produced. Instead of using the dark object database retrieval options, externally derived AOD values can be passed to the algorithm. More advanced processing options can be also modified, e.g., the environmental correction can be disabled, and either the multiple-scattering approximation or the simpler single-scattering approximation can be employed.

B. Cloud and Cloud Shadow Detection

We integrated a modified version of the Fmask algorithm [5], and we implemented the modifications described by [26], i.e., the discarding of the termination criterion for shadow

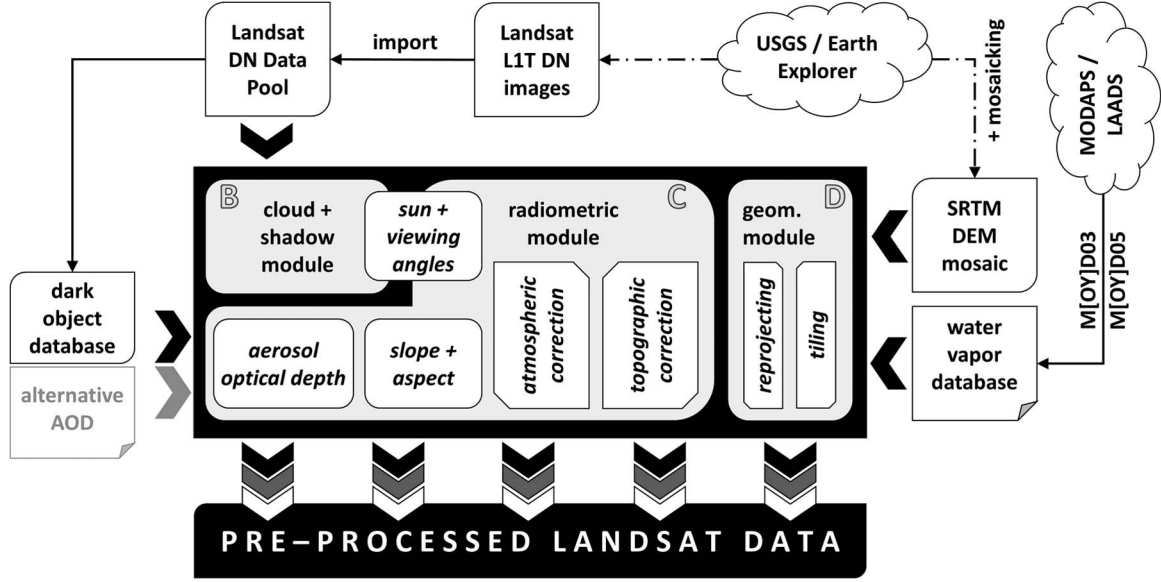


Fig. 3. Schematic workflow of the preprocessing framework. B, C, and D refer to the subsections of the methods section.

TABLE II
MATHEMATICAL SYMBOLS

Symbol	Meaning
λ	Wavelength
ρ, ρ^*, ρ_p	Surface reflectance, at-satellite reflectance, path reflectance
$\langle \rho \rangle$	Background contribution to the apparent target reflectance
θ_s, θ_v	Sun and view zenith angles
ϕ_s, ϕ_v	Sun and view azimuth angles
μ_s, μ_v	Cosine of θ_s and θ_v , indicating downwelling and upwelling terms, respectively
T, t_d, t_s	Total transmittance, direct transmittance, scattered (diffuse) transmittance
T_g, T_w	Total gaseous transmittance, water vapor transmittance
a_w, W, M	Water vapor absorption coefficient, precipitable water vapor, relative air mass
$L^*, d, ESUN$	At-satellite radiance, Earth-Sun distance, mean solar exo-atmospheric irradiance
A_p, R, g	Plane albedo, reflectance functions, asymmetry factor
τ, τ_a, τ_r	Total, aerosol and molecular optical depth
P, P_a, P_r	Total, aerosol and molecular phase functions
Ψ, s	Backscattering angle, spherical albedo
g_1, g_2, α	Asymmetry parameters of the TTHG function
$\rho_o, \rho^*, \rho_e, r$	Dark object reflectance, environment reflectance and target radius
ρ_s, ρ_w, ρ_f	Reference reflectance, volumic water reflectance, Fresnel reflectance
a_0, a_1, a_2	Coefficients of the logarithmic τ_a vs. λ regression
A, C	Topographic A- and C-Factors
$i, \cos i$	Incidence angle, illumination angle
b, m	Intercept and slope of linear regression between $\cos i$ and L^*
h, h_0	Portion of the sky dome which contributes to the diffuse illumination (h_0 : h at $\cos i = 0$)
θ_n, ϕ_n	Topographic slope and aspect

Definition of the mathematical symbols used in this paper.

matching and the inclusion of an additional darkness filter, as well as most of the Fmask updates [23]. In addition, we modified the match similarity metric for matching the clouds with their shadows. In the original Fmask code [5], a cloud is shifted along a projected search path, and a match between this projected shadow and potential cloud and cloud shadow layers is computed. The original cloud is excluded from the match. Nevertheless, if there is a big cloud in the search path, the

match similarity is maxed out, because the projected shadow is completely contained in the bigger cloud. Thus, the shadow matching often “runs” into the next big cloud, and the actual shadow is missed. Therefore, we only match the projected shadow with the potential shadow layer, which provides good results when combined with the disabling of the termination criterion [26].

Rather than buffering the cloud and cloud shadow objects, we calculate the distance to the next cloud or cloud shadow [27] for each pixel. This approach increases the flexibility of this data set regarding varying demands of different follow-up applications: the user can decide on how large the buffer should be for his specific application or can make use of the full distance information, e.g., [10] used the cloud distance in a PBC application to score the usability of a given observation by using a transfer function. We append the cloud/shadow pixel distance as seventh layer to the processed data (spectral information is stored in the first six bands).

In order to increase the computational performance, we implemented two full-stop criteria where the processing of an image is terminated after or within (before the costly shadow matching) the cloud detection module if the scene cloud coverage exceeds a given user-defined threshold. We set this threshold to 25% unbuffered cloud and cloud shadow cover.

C. Radiometric Processing

Following Tanré’s formulation for radiative transfer [28] and by adding a topographic correction factor A [12], [29], the surface reflectance ρ can be expressed as [30]

$$\rho = A \cdot (\rho^* / T_g(\mu_s, \mu_v) \cdot [1 - \langle \rho \rangle s] - \rho_p [1 - \langle \rho \rangle s] - T(\mu_s) t_s(\mu_v) \langle \rho \rangle) / (T(\mu_s) \cdot t_d(\mu_v)) \quad (1)$$

where ρ^* is the at-satellite reflectance, ρ_p is the path reflectance, and $\langle \rho \rangle$ is the background contribution to the apparent target

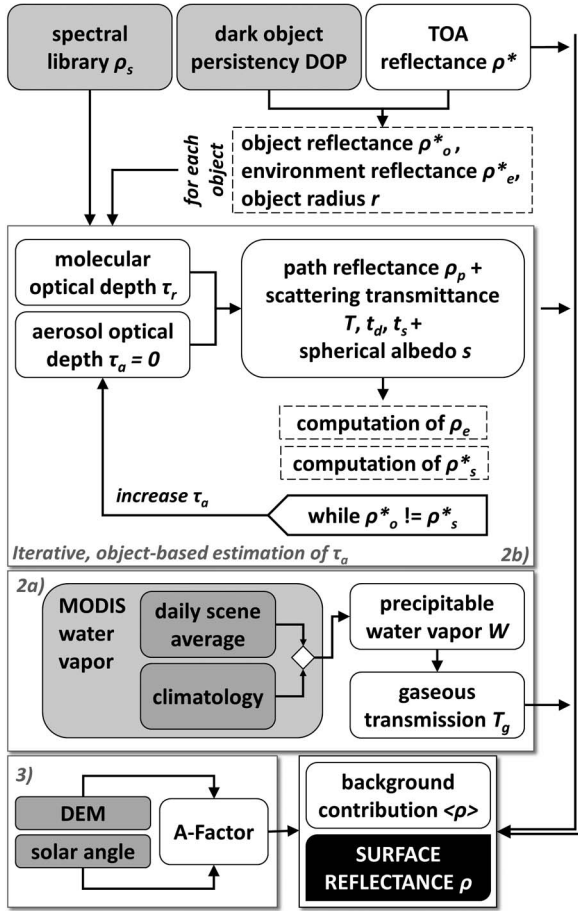


Fig. 4. Workflow for the radiometric processing. The subsections of this subsection are grouped in boxes.

reflectance. μ_s and μ_v are the cosines of the sun and view zenith angles Θ_s and Θ_v . $T(\mu_v)$, $t_d(\mu_v)$, and $t_s(\mu_v)$ are the total, direct, and scattered (i.e., diffuse) upwelling transmittances, respectively; downward transmission terms are indicated by their dependence on μ_s . $T_g(\mu_s, \mu_v)$ is the total gaseous transmission, and s denotes the spherical albedo. Most of the variables in (1) and the following equations are wavelength dependent; we omitted the wavelength subscript λ for the sake of simpler equations.

The adjacency effect is accounted for by the background contribution $\langle \rho \rangle$, which is derived from the weighted sum of the measured apparent reflectance around the target and from the target itself (see [30] and [31] for details).

A simplified schematic workflow for the radiometric correction module is shown in Fig. 4.

1) *DN to TOA Reflectance Conversion*: The TOA reflectance ρ^* of a tilted surface is computed by [32]

$$\rho^* = \pi \cdot d^2 \cdot L^* / (ESUN \cdot \mu_s). \quad (2)$$

The at-satellite radiance L^* is derived from the calibrated DNs by applying the rescaling factors which are included in the metadata [32]. The mean solar exoatmospheric spectral irradiance $ESUN$ was derived by applying sensor-specific relative spectral response (RSR) functions to the Thuillier solar

spectrum [32], [33]. Θ_s and the solar azimuth angle Φ_s , as well as the Earth–sun distance d [34], are computed by using the date and location from the metadata. Although it is generally accepted to only use the sun position at the scene center [9], we compute sun positions for square blocks of 333 Landsat pixels, which results in a roughly 10-km spaced sun position grid; the view zenith Θ_v and azimuth angles Φ_v are computed likewise.

2) *Atmospheric Correction*:

a) *Gaseous transmittance*: In our current implementation, we focus on the transmittance of water vapor absorption as first approximation. Among the radiance-modifying gases, water vapor is the most variable agent. The gaseous transmittance term in (1) then simplifies to

$$T_g(\mu_s, \mu_v) = T_w(\mu_s) \cdot T_w(\mu_v) \quad (3)$$

where the downwelling water vapor transmittance function is computed by [35]

$$T_w(\mu_s) = \exp(-0.2385 \cdot a_w W M(\mu_s) / [1 + 20.07 \cdot a_w W M(\mu_s)]^{0.45}) \quad (4)$$

which is dependent on the relative air mass M , on spectral water vapor absorption coefficients a_w , and on the precipitable water vapor W (measured in centimeters). The relative air mass M is defined as [35]

$$M(\mu_s) = \frac{1}{[\mu_s + 0.15 \cdot (93.885 - \theta_s)^{-1.253}]} \quad (5)$$

The upwelling water vapor transmittance is calculated by using Θ_v and μ_v instead of Θ_s and μ_s . We derived hyperspectral a_w values from the high-resolution transmission molecular absorption database [36] with the Landsat RSR functions.

Precipitable water estimates W are provided by a previously generated MODIS water vapor database. Therefore, we implemented an operational module for automatic data acquisition and processing of MODIS data. For each WRS-2 frame in continental subequatorial Africa, day-specific water vapor loadings are derived if possible. We determine spatial averages from all cloud-free and sun-glint-free pixels within the WRS-2 footprints, separately for the Terra and Aqua granules. If estimates from both sensors are available, we choose the one with the larger number of valid pixels, which, in most cases, is Terra for Landsat-7 (99.4%) and Aqua for Landsat-5/8 (99.2%) due to orbital characteristics. If there are less than 10% of valid pixels, the average is expected to be unreliable, and we fall back on an alternative parameterization, which applies for missing data of any kind, including the pre-MODIS era, coverage gaps between the swaths, and sensor outages. Southern African climate is dominated by a stable and pronounced seasonality into a dry and wet season. Therefore, W is replaced by an average seasonal proxy derived from a statistical analysis of the complete MODIS water vapor data sequence—if necessary. This fallback climatology was used in 100% of all cases before 2000, 25.3% in 2000, 2.2% in 2001, 2.8% in 2002, and less than 0.4% thereafter, which reflects the phased commissioning of the Terra and Aqua platforms. Exemplary water vapor data

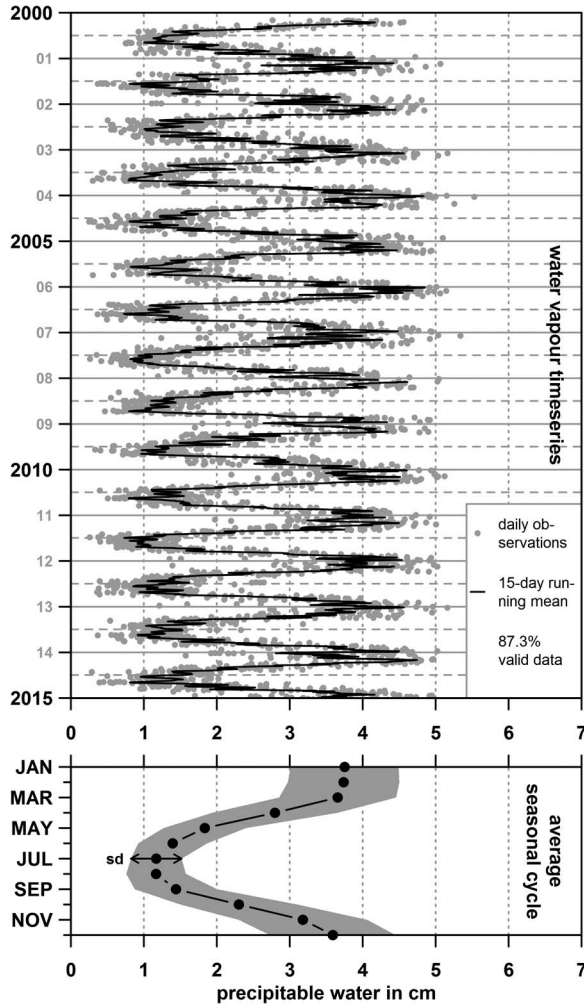


Fig. 5. Visualization of the water vapor database for WRS-2 Path/Row 177/072 (19.71° E, 17.35° S). (Top) Daily values and 15-day running mean. (Bottom) Average seasonal cycle and standard deviation on monthly basis.

are plotted in Fig. 5 for WRS-2 Path/Row 177/072, with daily values in the top panel and the fallback climatology at the bottom panel. Water vapor follows a seasonal cycle with low values in the dry season and high values in the wet season. The standard deviation is higher in the wet season, which could indicate that the error in using the fallback values is smaller during the dry season during which Landsat data availability is higher. In order to document the usability of this approach across the study area, we appended additional examples in the supplemental material section of this paper. We chose the Landsat frames with the highest monthly average and standard deviation. The seasonal and annual variability is higher in the latter example (compared with Fig. 5), but a seasonal pattern is evident nonetheless. In addition, we provide maps of the fallback climatology (see the bottom panel in Fig. 5 for one frame) for complete subequatorial Africa in the supplemental material section.

b) AOD: i) Radiative transfer theory

All remaining unknown parameters in (1) can be derived from AOD τ_a [30], [37], by either using the single-scattering approximation [38] or by also considering multiple-scattering

processes [39]. Equations (6)–(19) provide the derivation of these atmospheric scattering terms from τ_a using the multiple-scattering approach (refer to [37] for the simpler single-scattering approximation). The practical estimation of τ_a is outlined in the following subsections (ii–iv).

The path reflectance ρ_p is defined by an exact treatment of first-order scattering and an approximate solution for higher order scatterings, i.e.,

$$\rho_p = A_{pl} + [3(1+g)\mu_v\mu_s - 2(\mu_v + \mu_s) + P] \cdot [1 - \exp(\tau/\mu_v - \tau/\mu_s)] / [4(\mu_v + \mu_s)]. \quad (6)$$

The plane albedo A_{pl} is given by [40]

$$A_{pl} = 1 - R(\mu_v) \cdot R(\mu_s) / (4 + 3(1-g)\tau) \quad (7)$$

where the reflectance functions $R(\mu_s)$ (replace μ_s with μ_v to obtain $R(\mu_v)$) are given by [40]

$$R(\mu_s) = 1 + \frac{3}{2}\mu_s + \left[1 - \frac{3}{2}\mu_s\right] \cdot \exp(-\tau/\mu_s) \quad (8)$$

with the asymmetry factor [41]

$$g = [\alpha \cdot (g_1 + g_2) - g_2] \cdot \tau_a / \tau. \quad (9)$$

The total optical depth

$$\tau = \tau_a + \tau_r \quad (10)$$

is the sum of τ_a and the molecular optical depth τ_r for a standard Rayleigh atmosphere [42], i.e.,

$$\tau_r = 0.0088 \cdot \lambda^{-4.15+0.2\lambda}. \quad (11)$$

The total phase function

$$P = P_a \cdot \tau_a / \tau + P_r \cdot \tau_r / \tau \quad (12)$$

for the backscattering angle

$$\psi_- = \cos^{-1} \left\{ -\mu_v\mu_s - [(1-\mu_v^2)(1-\mu_s^2)]^{0.5} \cos(\phi_v - \phi_s) \right\} \quad (13)$$

is obtained from the phase functions for molecular [43]

$$P_r = 0.75 \cdot (1 + \cos^2 \psi_-) \quad (14)$$

and aerosol scattering P_a . The aerosol scattering equation is approximated by a two-term Henyey–Greenstein (TTHG) function, with $g_1 = 0.836$, $g_2 = 0.537$, and $\alpha = 0.968$, representing a continental aerosol model [41], i.e.,

$$P_a = [(1-g_1^2) \cdot \alpha] / [1+g_1^2-2g_1 \cos \psi_-]^{1.5} + [(1-g_2^2) \cdot (1-\alpha)] / [1+g_2^2-2g_2 \cos \psi_-]^{1.5}. \quad (15)$$

The downwelling total scattering transmittance

$$T(\mu_s) = \exp(-(0.52\tau_r + 0.167\tau_a)/\mu_s) \quad (16)$$

and the direct portion

$$t_d(\mu_s) = \exp(-\tau/\mu_s) \quad (17)$$

and the scattered portion

$$t_s(\mu_s) = T(\mu_s) - t_d(\mu_s) \quad (18)$$

are readily computed (the upwelling terms are retrieved by replacing μ_s with μ_v). The spherical albedo s , viewed from the ground, is given by

$$s = \exp(-(\tau_r + \tau_a)) \cdot (0.92\tau_r + 0.333\tau_a). \quad (19)$$

Thus, solving (1) only requires a robust estimation of τ_a , which, in the absence of measurements, is commonly derived from the image itself with dark target techniques, assuming that candidate objects exist in every image (e.g., [37]).

ii) DODB

For the practical implementation of this concept, we utilize a partially image-based approach by using a precompiled dark object database (DODB). The DODB is created from the complete data series of each pixel and guarantees that the dark objects (DOs) are estimated from the same pixels for all bands and that, preferably, the temporally more persistent ones are used for estimating τ_a . This prevents that temporary DOs (such as flood water, burned areas, or cloud shadows) are used in some images, whereas completely different DOs are used in other images that do not contain such objects.

The generation of the DODB is a prerequisite for our pre-processing algorithm; thus, we based the generation of the DODB on an analysis of the DNs of every available image. DOs are identified in each image by using the red and NIR band histograms (see next paragraph). After all the individual images are analyzed, the DO persistency (DOP; with DOP = [0, 100], i.e., the percentage of the time a pixel is dark) is derived for each pixel in the study area. In order to account for potential land cover change during the past 30+ years, we compiled three decadal databases, i.e., [1984, 1995], [1996, 2005], and [2006, 2015]. The DODB is designed such that newly acquired data can be simply integrated into the database by updating the DOP score. Fig. 6 displays a subset of the DOP, as well as two examples of Landsat false-color images for an area that is characterized by varying water levels [more water during the late wet season (middle panel)] and the presence of burn scars [more likely during the course of the dry season (bottom panel)]. The use of the most persistent DOs effectively prevents the usage of the transient dark features, in this case, the flood plains and the burned areas, which were also marked as DO in some images (b/w tones in the top panel).

We identify DOs in the red and NIR bands for each processed image. The NIR band is utilized because of the decreasing scattering effect at longer wavelengths [44], which increases the darkening effect of shadowed pixels [5], and because most surface features are bright and thus maximize the contrast to shadowed areas [5]. The red band is used to reject highly turbid water bodies. For both bands, the DOs are retrieved from the lower bounds of the band histograms.

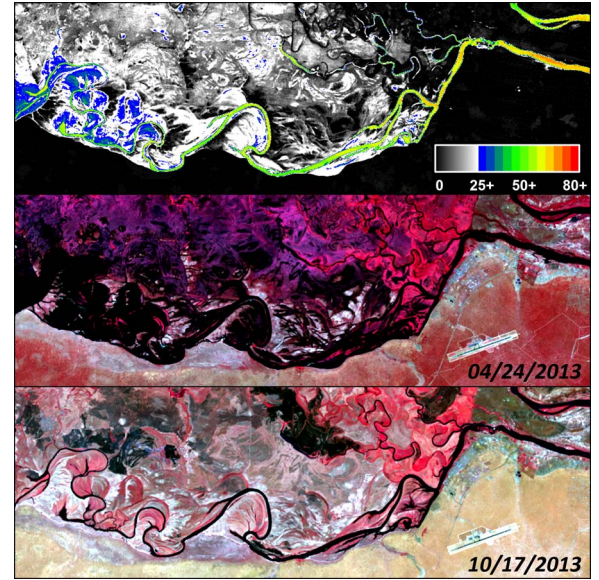


Fig. 6. Visualization of a section of the DODB and two example images (25.06° E, 17.79° S). (Top) DOP. (Middle) False-color image of a late wet season image. (Bottom) False-color image of a dry season image. The same stretch was applied to both images with R/G/B = NIR/red/green.

iii) Image-based estimation of AOD

Based on the persistent DOs, we employ an object-based approach where it is attempted to derive τ_a for each nontransient DO on a physically sound basis, implicitly including the adjacency effect. During the actual radiometric processing, the DOP is available to the algorithm and is used in combination with the ρ^* image under consideration. We only use pixels with consecutively decreasing ρ^* for all bands, which represents an important property of an ideal DO as it should follow a λ^{-x} relation [45]. Objects with less than 10 valid pixels or that are in close proximity to clouds (< 10 pixels) are discarded. The object reflectance ρ_o^* , environment reflection ρ_e^* , and target radius r are directly inferred from the image, the target altitude is considered by adjusting τ_r [42], and the objects are separated into water and topographic shadow targets based on the illumination situation. If ρ_e^* is smaller than ρ_o^* , the object is rejected.

Our approach builds on the method of [46], where ρ_o^* is matched with the spectral reference reflectance ρ_s^* of a typical DO. In case of water, the surface reference reflectance is given by

$$\rho_s = \rho_w + \rho_f t_s(\mu_s)/T(\mu_s) \quad (20)$$

with ρ_w being the volumic water reflectance that is obtained from a spectral reference library (see in the following). The Fresnel surface specular reflectance ρ_f is computed as a function of the incidence angle i [47], assuming that water surfaces are flat. AOD is determined in a bandwise iterative procedure by gradually adding atmospheric scattering to ρ_s , thus simulating the reference reflectance ρ_s^* as it would be sensed at the top of the atmosphere [solve (1) for ρ^* with $A = 1$ while increasing τ_a , starting with a pure Rayleigh atmosphere, i.e., $\tau_a = 0$]. This process terminates once ρ_s^* and ρ_o^* match (see [46] for a detailed description). In the case of cast shadow, we use a

modified version of this approach where ρ_f is ignored but the topographic correction factor A (see topographic correction) is included in order to model the shaded ρ_s^* . The procedure is outlined in Fig. 4 in simplified form.

In order to obtain a more physically coherent set of the wavelength-dependent τ_a , to reduce measurement-dependent variations [30], and to have an instrument for gauging the quality of the estimation (R^2) [46], we perform a logarithmic regression between τ_a and λ . A second-order polynomial fit is employed, i.e.,

$$\ln \tau_a = a_0 + a_1 \cdot \ln \lambda + a_2 \cdot (\ln \lambda)^2 \quad (21)$$

which enables the modeling of the inherent $\ln \tau_a$ curvature of biomass burning and desert dust aerosols as a consequence of accumulation mode dominating aerosol size distributions [48]. If unsuccessful (e.g., if the Ångström exponent $a_1 > 0$), the simpler linear Ångström relation [49] is tried in a second step, where the second-order term in (21) is ignored ($a_2 = 0$). If the fit to the Ångström equation is also unsuccessful (e.g., if $a_1 > 0$), the object is rejected.

Due to the profound variability of naturally occurring water bodies/land surfaces, we precompiled spectral reference libraries (for a range of possible conditions) using spectral modeling software. The water color simulator WASI [50] and the leaf optical properties + canopy bidirectional reflectance model PROSAIL [51] are used for the water and cast shadow targets, respectively. For each object, each reference spectrum ρ_s is tested, and the corresponding τ_a estimate that yields the best R^2 in the logarithmic regression is retained; if the best R^2 is smaller than 0.1, the object is rejected.

As dark targets are not abundantly available across the images in our study area [52], we compute a τ_a scene average from all available targets, weighted by the R^2 of the logarithmic regressions, while considering the individual target altitudes [42]. Once τ_a is retrieved, the governing equation [see (1)] can be solved by computing all parameters, as described in the radiative transfer theory subsection, using (6)–(19). We introduce some scene fidelity by using coarsely gridded (333 pixels) sun-target-view angle dependencies that allow the scattering equations to vary over the scene. In addition, τ_a and τ_r are adjusted for the pixel's altitude [42] in order to approximate the elevation dependence on the optical depths.

iv) Fallback strategy

The African savanna landscape is often bright [53], and a substantial number of Landsat footprints do not contain dark targets (all objects were rejected, see previous section), in which case, we cannot retrieve τ_a and consequently employ an alternative fallback strategy in a second step.

We implemented a backdoor interface, where externally generated τ_a values can be passed to the algorithm. In this case, the image-based estimation of τ_a is skipped, and the external values are used instead. We made use of this possibility for the images where we could not identify any valid dark target and reprocessed these images with modeled τ_a values. This applied to ~14% of the images and particularly occurred in the bright landscapes of southern Namibia and Botswana.

We used the τ_a values of all the images where the presented method (see the “image-based estimation of AOD” subchapter) worked well and modeled the climatic seasonal course of τ_a with a dependence on geolocation: we used a multivariate regression model described by the geolocation and the acquisition day of years of the available τ_a values to estimate a set of spatiotemporal τ_a fallback values with a revisited version of [52] (direct modeling of τ_a instead of ρ_p).

3) *Topography Correction*: Topography correction is done by applying a modified C-correction [12], which is a physically based correction of topography, amended by an empirically derived extra parameter C [54]. The topographic correction factor in (1) is determined for every image, band, and pixel, i.e.,

$$A = \frac{(\cos \theta_s + C \cdot h_0^{-1})}{(\cos i + C \cdot h_0^{-1} h)}. \quad (22)$$

The illumination angle $\cos i$ is computed by [55]

$$\cos i = \cos \theta_s \cos \theta_n + \sin \theta_s \sin \theta_n \cos(\phi_s - \phi_n). \quad (23)$$

The topographic slope θ_n and aspect ϕ_n are computed with the Horn method [56] from the DEM that was warped to the extent and resolution of the Landsat image under consideration. The h -factor describes the portion of the sky dome which contributes to the diffuse illumination, where h_0 is the h -factor at $\cos i = 0$ [12]. The C -factor is estimated from a linear regression between $\cos i$ and the spectral radiance from an inclined surface L^* . The empirically derived C -factor is then the ratio of intercept b and slope m , i.e.,

$$C = \frac{b}{m}. \quad (24)$$

The main focus of attention in computing the A -factor is to derive this C -factor. Because of the image-based nature of this correction, we were in need of incorporating several stabilizing constraints in order to estimate the C -factor in a robust manner for preferably all images, as follows.

- The results of the C-correction can be improved if the C -factor is not derived for the entire Landsat image, but separately for different land cover classes [12]. Thus, we split the image pixels into two classes based on an arbitrary normalized difference vegetation index threshold of 0.4 [54].
- If there is no equal abundancy of differently illuminated pixels, the regression-based correction often fails to be representative for all topography classes and results in significant undercorrection/overcorrection. Reference [54] used a threshold of 2° slope angle for excluding rather flat pixels. We found that this method worked in many cases, but depending on image content, this constraint is often not sufficient for Landsat frames with unequally mixed and complex terrains. In our operational setting, we found it very effective to also stratify the image with 5° slope classes. Thus, we estimate the C -factor for each land cover and slope class separately.

- If the coefficient of determination R^2 is less than 1% in a given class, we assume that the C-correction did not perform well and we fall back on a simple Minnaert correction [29] with a fixed Minnaert coefficient of 0.8. This simplifies the A -factor to

$$A = \left(\frac{\cos \theta_s}{\cos i} \right)^{0.8}. \quad (25)$$

The relationship between L^* and $\cos i$ is in general not very high; [12] reported R^2 values between 5% and 30% for the different bands of their testing image. Such high R^2 values are not always given if the image is not entirely mountainous; thus, we set the threshold to 1% to test if there is at least any evidence of a relation. The class-dependent topographic correction approach implies that one image may be corrected with different methods, giving precedence to the more advanced C-correction as it commonly comes off as winner in comparative topographic studies, e.g., [54].

D. Reprojection and Gridding

Once the Landsat data are radiometrically corrected, they are reprojected into the output coordinate system using bilinear resampling and second-order polynomial warping. For our study data, we chose a Lambert azimuthal equal area (LAEA) projection with its origin in the centroid of southern Africa. After reprojection, the data are organized in smaller arbitrary tiles. Therefore, a grid in the target projection is created. The grid originates at a custom point O_{grid} , and a new tile is created each n_{grid} pixels. For our study area, we chose the arbitrary grid to origin at $O_{\text{grid}} = 0^\circ/0^\circ$ in latitude/longitude, and n_{grid} was chosen to be 1000 pixels in the LAEA projection. In order to avoid confusion about nomenclature, we hereby define the following terms:

- “grid” as an arbitrary subdivision with square units in the target coordinate system;
- “tile” as an entity of the grid with a unique tile identifier, e.g., X0003_Y0002;
- “chip” as the individual gridded images that are affiliated with the tile.

The disintegration of the classical Landsat WRS-2 data structure into a new gridded tile representation has several benefits: easy and rapid pixel-based data access, simple coregistration among images, regardless of their initial path and row designation, and thus exploiting the full depth of the Landsat archive, as well as easier ordering of data for study areas that commonly match imperfectly with WRS-2 frames.

V. RESULTS

A. Processing Stats

We processed 58 731 Landsat images of 194 WRS-2 frames with the presented method. Fully processed were 41 762 images; 16 876 images were terminated in an early stage because

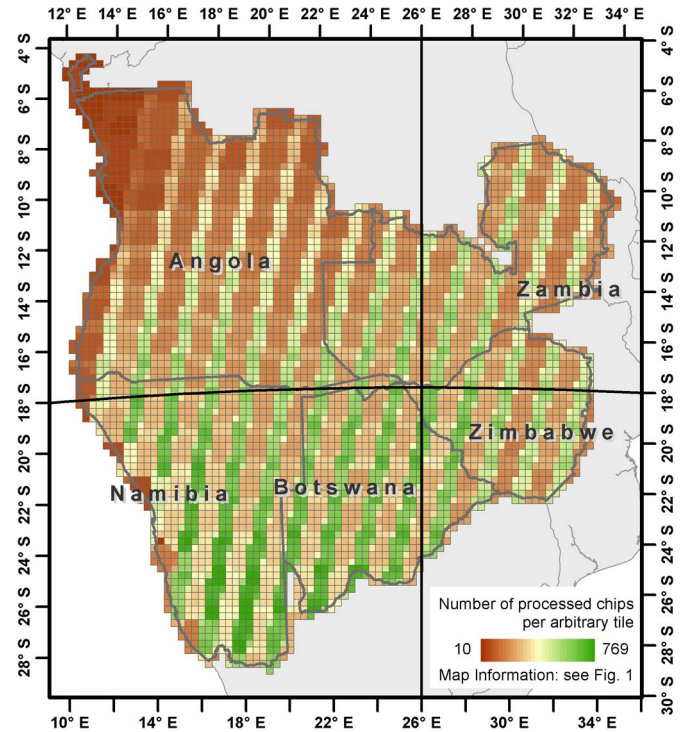


Fig. 7. Number of processed chips per arbitrary tile, corrected for redundant overlaps.

the cloud contamination exceeded the maximum allowable cloud cover threshold, and 90 images were so far not processed because of a recent failure in the thermal infrared sensor (TIRS) calibration. The processed images were partitioned into 4524 tiles and 1 912 733 chips, resulting in a total data volume of 27.86 TB. The core processing was finished in less than four days on a moderately sized processing cluster (two nodes and 56 central processing units). Fig. 7 displays the number of processed chips per tile. The data availability—corrected for redundant data—is highest in the overlap region between two orbits.

B. Spectral Consistency in Overlap Regions

Our gridded data structure enables us to analyze the spectral consistency within three types of overlapping image regions.

- LPGS generates redundant data in the overlap region of adjacent WRS-2 frames that were captured in the same orbit. Thus, any difference in this redundant overlap should be caused exclusively by the implemented processing chain and enables the exploration of the inherent systematic errors/uncertainties.
- The revisit overlaps between two adjacent orbits are captured seven days apart by the same Landsat system. The data might vary somehow due to different atmospheric situations and oppositional viewing directions, which we assume to have the greatest impact. In addition, rapid phenology processes, as well as process-based change such as changing water levels, burned areas, or active fires, might add to the difference.

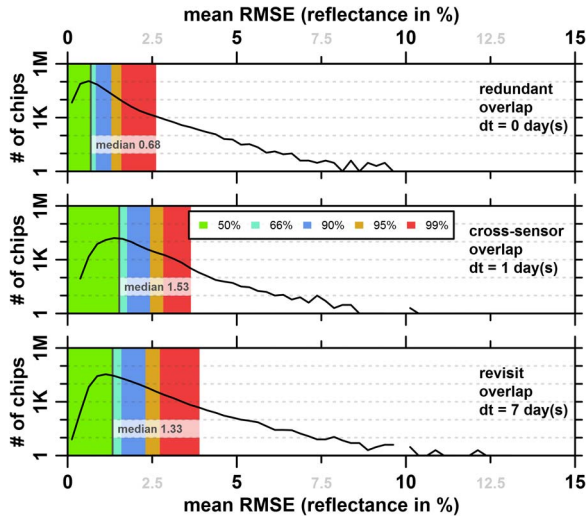


Fig. 8. Histograms of the spectral consistency assessment of overlapping chip pairs. The histogram bin width was set to 0.25% reflectance. The y -axis is drawn logarithmic. Quantiles are drawn in colors.

- The observation frequency reduces to one day in the cross-sensor overlaps if data from several sensors are considered, although the viewing aspect angle is still substantially different. A comparison between the one-day and seven-day differences might be useful to differentiate between the cross-sensor uncertainties and differences that are caused by surface processes.

The assessment is based on an exhaustive analysis of all overlapping chips. The spectral consistency for every chip pair was assessed by the spectral root mean squared error (RMSE) of the six reflective bands b , averaged over all overlapping pixels p , i.e.,

$$\text{meanRMSE} = \frac{1}{n} \sum_{p=1}^n \sqrt{\frac{1}{6} \sum_{b=1}^6 [\text{chip1}_{p,b} - \text{chip2}_{p,b}]^2}. \quad (26)$$

In order to avoid situations with unlike atmospheric conditions, we omitted pixels that are located within a 10-km radius from clouds or cloud shadows.

Fig. 8 displays histograms of this assessment for the three overlap types. Quantiles are drawn in colors. The differences in the redundant overlaps are smallest: the mean of the revisit (cross-sensor) overlaps is 0.70% (0.84%) larger than that of the redundant overlaps. The error in the cross-sensor overlaps is usually larger than that in the revisit overlaps (0.14% difference in the mean), although the 99% quantile is slightly smaller. The expected accuracy of the full radiometric processing chain is on the order of $\pm 2.5\%$ reflectance [57]. Within this range are 98.8% of all redundant chip pairs. Considering the orbital overlaps, still 92.8% (91.0%) of the revisit (cross-sensor) chip pairs are enclosed.

C. AOD

Sunphotometer data from the Aerosol Robotic Network (AERONET) [58] are commonly considered the most accurate

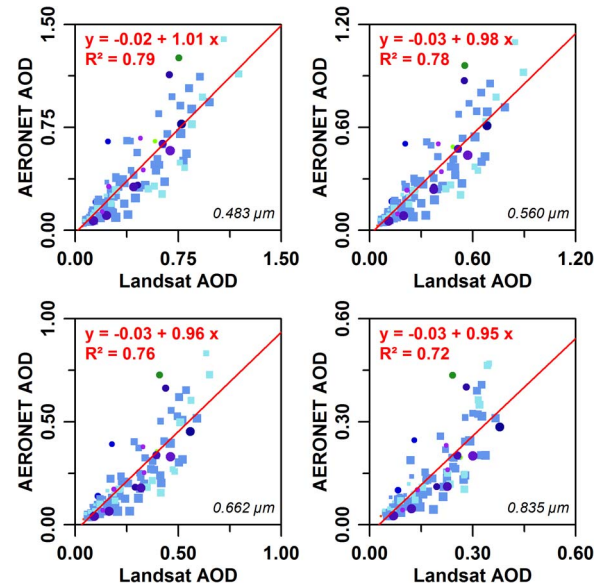


Fig. 9. Linear regression between image-based Landsat and terrestrial AERONET AOD measurements for all stations and all coinciding observations. The colors represent different AERONET sites: blue to purple—Zambia; red/orange—Namibia; green—Botswana. The majority of the data are from the Mongu sites, Zambia.

terrestrial τ_a measurements, and as such, we derived Landsat-equivalent τ_a from all available AERONET data in our study area with (21). The relationship (R^2) between the satellite-based and coinciding ground-measured τ_a is between 0.72 and 0.79 for all bands (see Fig. 9), intercepts are on the order of 0.02–0.03, and the relationship is very close to the 1-to-1 line. The colors represent different AERONET sites (blue colors: Zambia; red colors: Namibia; green colors: Botswana; no stations for the remaining countries), and the point sizes indicate the mean DOP of the dark targets. The majority of the observations are from the two Mongu sites (23.15° E, 15.25° S), which are drawn as rectangles.

The fallback surface, i.e., the spatiotemporal aerosol climatology, was modeled from all available τ_a estimates across the whole study area (see [52] for details). With regard to the quality of the aerosol climatology, [52] found that the modeled seasonal aerosol cycle matches well with an average seasonal cycle derived from the AERONET Mongu station. An updated assessment of this relationship is included in the supplemental material section of this paper, with R^2 between 0.81 and 0.84 for all bands.

D. Uncertainty in Climatic Water Vapor Database

If daily water vapor values are not available, we rely on a fallback climatology. In order to better understand the potential error and document the uncertainty in using this method, we simulated the potential effect of varying water vapor concentrations. The effect of water vapor absorption is albedo dependent. Therefore, we picked a Landsat frame which includes both bright and dark surface elements. The Etosha pan is a large salt pan without drainage. The pan is normally very bright, but it can be partially flooded after heavy rain, and the water can be retained during the course of the dry season. The

TABLE III
PRECIPITABLE WATER VALUES

Water vapor variant		Dry season 08/10/2008	Wet season 03/22/2009
Daily value	DV	1.02	2.32
Climatic average - 2 sd	CA--	0.29	1.96
Climatic average - 1 sd	CA-	0.70	2.85
Climatic average	CA	1.12	3.74
Climatic average + 1sd	CA+	1.53	4.63
Climatic average + 2sd	CA++	1.95	5.52

Precipitable water value variants (in cm) used for simulating the effect of climatic averages on the corrected reflectance of different land surface types.

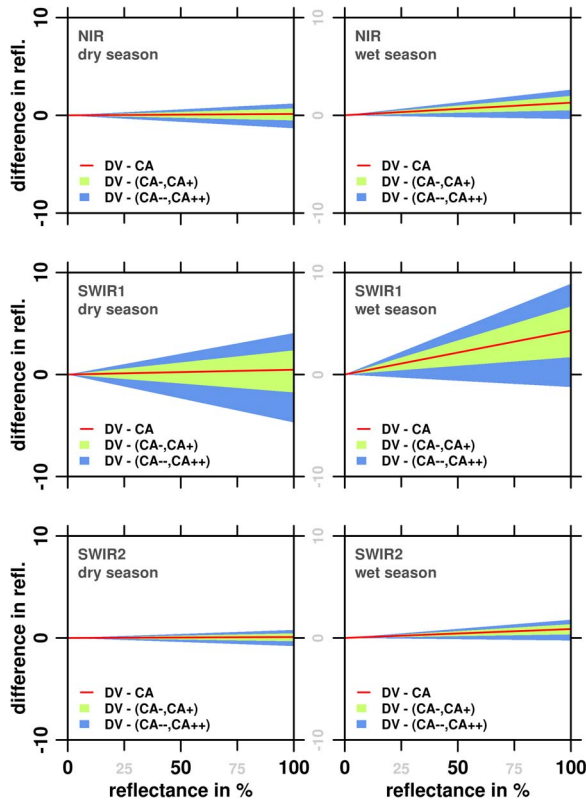


Fig. 10. Potential errors in using climatically derived water vapor estimates instead of daily values. The analysis was performed with two dry/wet season TM images of the Etosha Pan. Both images were corrected with different water vapor values (see Table III). The figure displays the difference in surface reflectance (in %) between the correction with day-specific values and the correction with climatically derived variants.

analysis is based on Landsat-5 data since the TM is the most water vapor impacted Landsat sensor because of its spectral configuration. We chose two cloud-free images that captured a partially flooded pan, one in the dry (08/10/2008) and one in the late wet season (03/22/2009).

We corrected each image with the retrieved daily water vapor values (DV) and with the corresponding climatic average (CA), which would be used in case the daily value would not be available. In addition, we also increased and decreased the climatic average by one and two standard deviations (see Table III). We base our analysis on the resulting difference in surface reflectance between the DV and the climatic variants (see Fig. 10). The impact of water vapor is small on the NIR and SWIR2 bands, but clearly evident in the SWIR1 band;

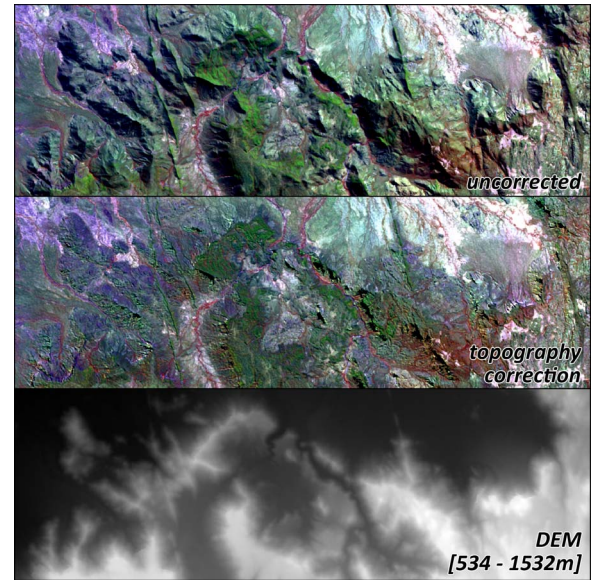


Fig. 11. Illustration of the topography correction for a mountainous Landsat-8 image in Huila, Angola (13.39° E, 15.86° S; 1000-m elevation range) under low-illumination conditions (sun elevation: 41° , azimuth: 37°). (Top) No topography correction. (Middle) Topographically corrected. (Bottom) DEM. The same stretch was applied to both images with R/G/B = NIR/SWIR1/red.

the VIS bands are hardly affected and thus not displayed here. The effect is more pronounced for very bright surfaces. The daily water vapor estimate of the dry season image is very similar to the climate average, whereas the daily estimate in the wet season is approximately 1.5 standard deviations smaller than the climate average. Thus, the corrected reflectance differs by 0.53% (4.8%) between the DV and the CA for the dry (wet) season image for extremely bright features (100% reflectance). The effect is less pronounced for gray objects (50% reflectance): 0.29% (2.6%) difference. For the SWIR1 wet season images, the difference in corrected reflectance between the CA+ (CA++) and CA- (CA--) variants is approximately 3% (6.2%) for gray objects. In the dry season, the differences are 2.6% and 5.6%, respectively; thus, the uncertainty in the wet season is slightly higher.

E. Topographic Correction

Fig. 11 illustrates the implemented topographic correction for an illustrative sample area. The depicted images were captured over the mountainous Huila province (southern Angola) in the middle of June (winter solstice) under low-illumination conditions (sun elevation: 41°). The elevation ranges between 534 and 1532 m. Topographic effects were substantially reduced, and the corrected image appears to be rather flat.

Fig. 12 demonstrates the effectiveness of the topographic correction by averaging the NIR reflectance (separately for both land cover classes) with dependence on the topographic aspect. The illumination direction (sun azimuth: 37°) is clearly visible in the uncorrected image (red), whereas the effect is substantially reduced in case of the C-correction (green). In order to show the advantage of our method over the simpler fallback option, we also corrected this image with the Minnaert correction (blue), which has a tendency for overcorrection.

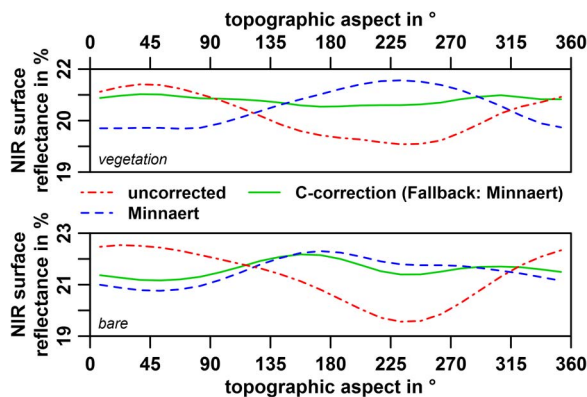


Fig. 12. Average aspect-dependent NIR reflectance for the image (full frame) shown in Fig. 11 for the (top) vegetated and (bottom) bare classes. The image was processed with the implemented C-correction (green), the Minnaert correction (blue), and with disabled topography correction (red). Flat curves point to a successful topographic normalization.

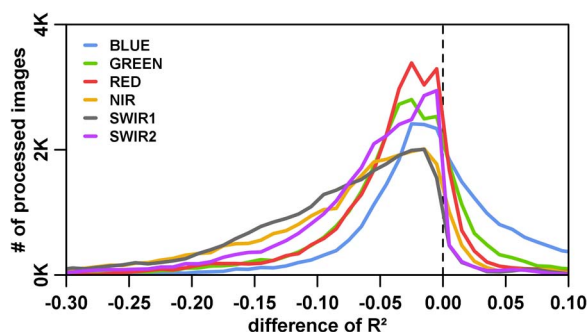


Fig. 13. Topographic correction evaluation. The histogram bin width was set to 0.01 R^2 . The correction was quantitatively evaluated by differencing the R^2 of the relationship between $\cos i$ and L , before and after the radiometric correction. A decrease in R^2 points to a reduction of topographic effects.

The topographic correction was quantitatively evaluated by comparing the R^2 of the relationship between $\cos i$ and L , before and after the radiometric correction. Fig. 13 displays histograms of the difference in R^2 . All images with more than 10% of sloped terrain ($> 5^\circ$) were used to derive the histograms. R^2 usually decreases after the correction. The strength of the decrease is different for the six spectral bands. The R^2 of the blue band occasionally increases after the correction, and the decrease is more apparent in the infrared bands.

VI. DISCUSSION

A. Data Set Consistency

We mainly based the quantitative assessment of the data set on an exhaustive analysis of all overlapping chip pairs, which enables us to gauge the processing consistency. The differences between processed redundant data are attributed to our processing chain. These differences are usually very small, and 98.8% of all overlaps were within the expected 2.5% algorithm accuracy [57]; 99.4% differ by less than 3%. The differences between the chips are likely to be caused by the image-based methods, where different image contents can cause different AOD retrievals. As such, we conclude that the

AOD estimation strategy worked reasonably well (see also the next subsection), and we expect our processing chain to be of sufficient quality for any following pixel-based compositing or time series analysis application.

The revisit and cross-sensor overlaps are captured on different dates and inhibit different orbital characteristics, different atmospheric states, and, potentially, land surface change. We presume that opposite view angles have the greatest impact since we do not correct for BRDF. The differences are indeed greater than in the redundant overlaps. Therefore, we assume that the part of the BRDF, attributed solely to the different viewing geometries (which we partially account for by considering the varying sun-target-view geometry in the atmospheric scattering terms), is in the dimension of this difference, i.e., $< \sim 1\%$ reflectance. As the sun geometry does not change significantly during this time period, we are not able to assess the actual combined effect of BRDF with the performed overlap analysis, although the impact on our data set is likely to be significantly larger, as recently documented by [59]. Accounting for BRDF effects is complex and not yet a standard correction for Landsat data. An optimal BRDF correction would estimate pixel-based bidirectional parameters by using many observations within a short time period [60]—an approach which is not applicable to Landsat data alone [14]. In addition, the parameter estimation with high temporal and coarse spatial resolution data is also problematic in arid areas during the wet season [61]. Thus, the transfer from MODIS-based bidirectional parameters to Landsat data (e.g., [62]) is also restricted in such environments due to the insufficient angular sampling in parts of the year. One notable and promising approach is to infer a globally applicable set of bidirectional parameters by implementing a sampling design, where pixels from a broad range of differently sloped and illuminated pixels in the Landsat orbital overlaps and in different land cover classes are selected [14]. Nevertheless, *a priori* knowledge about the land cover, a confident guess about the spectral stability over time, and sufficient input data are needed—demands that are still not met everywhere.

Based on a comparison of the two orbit overlap variants, we might be able to differentiate between the cross-sensor introduced error and changes that are attributed to surface change processes (e.g., green flush events, fire, or flooding), because the probability of surface change is higher in the revisit case. In general, the cross-sensor overlap differences were larger than the ones in the revisit overlaps. Thus, we conclude that surface change has less impact than cross-sensor calibration errors on average. As an exception to this, the 99% quantile was larger in the revisit overlaps, which could point to surface change. This implies that surface change happens rarely (within seven days), but if it does, it has a large impact on the differences of overlapping data. The cross-sensor errors might be amplified by the slightly different spectral configurations of the OLI sensor—compared with TM and ETM+. Reference [63] has recently found that the error in surface reflectance is around 2%, which also partially conforms to our results. The mean cross-sensor error is 1.64%, although the errors between overlapping Landsat-7 and Landsat-5 (1.67%)/Landsat-8 (1.60%) chips do not differ significantly in our case, and the OLI-to-ETM+ error

is even slightly smaller than the TM-to-ETM+ error. This might be due to the improved radiometric characterization of the OLI, compared with the TM, or presumably another yet unexplored factor.

B. AOD

The estimation of AOD in bright landscapes is a difficult task, and the absence of DOs on a large scale might preclude the usage of image-based assessments [64]. Reference [14] mitigated this problem by using a fixed AOD for Eastern Australia. While this is a sound strategy if the AOD is expected to be rather low, errors are inevitably included if the actual aerosol content is high [65]. The AOD in southern Africa is particularly variable [52] due to the accumulation (washout) of aerosols during the dry burning (wet rain) season [66] and regularly assumes large values (see Fig. 9). Therefore, we developed a method where the image-based DO retrievals were amended by temporal information on the persistency of DOs. This approach supports the use of the temporally more persistent DOs, which helped to increase the quality of the AOD retrievals in an environment where few DOs exist. Transient DOs such as burned areas were thus successfully rejected.

We used AERONET data to gauge the quality of our AOD estimation strategy. Unfortunately, few AERONET sites exist in the study area; the majority of the stations are confined to Zambia; there also exist three (two) stations in Namibia (Botswana), but no station exists in Angola and Zimbabwe. In addition, most of the stations also have very few high-quality Level-2 data. Most of the data are constrained to the two sites in Mongu, Zambia. Fortunately, this location is relatively central in the study area.

It was shown that our physically based AOD estimation on the basis of radiative transfer theory is in very good agreement with available AERONET data (see Fig. 9): R^2 ranges between 0.72 and 0.79, intercepts are low, and slopes are near unity. Despite being mainly driven by the Mongu observations (square signatures), the few observations from the other stations (point signatures) also fit reasonably well (see Fig. 9). We therefore expect that the calibrated AOD retrievals are reasonably accurate in areas with similar climate and landscape composition as the sites with AERONET coverage, which are particularly the wooded and forested regions in Angola and Zambia. It cannot be ruled out that the errors in the more arid ecosystems are larger and there is still a considerable amount of images (14%) where this strategy did not work due to the high albedo and dryness of savannas and deserts. We reasonably accounted for this with the fallback strategy by using modeled values [52]. We consider these values as an acceptable guess for the actual AOD in a spatially and temporally explicit manner (see [52] and the supplemental material of this paper).

Due to the aforementioned difficulties and environmental constraints, we recognize that AOD might still be one of the major uncertainties with regard to the quality of our data set. Nevertheless, we assume the AOD estimations and the AOD climatology to be sufficiently precise to give a reasonable characterization of atmospheric scattering in this highly variable ecosystem.

C. Water Vapor

It was shown that the effect of water vapor is small in all but the SWIR1 bands. TM is the most impacted sensor with regard to water vapor because the SWIR1 band is substantially influenced by water vapor absorption. The OLI sensor, in turn, is hardly affected by water vapor absorption because the SWIR1 band was substantially reduced and was moved well away from the absorption band. It was shown that the difference in using a climatically derived water vapor value was approximately 2.6% reflectance for gray wet season objects if the daily value is approximately 1.5 standard deviations smaller than the climatology. It was also shown that the uncertainty in using the climatology fallback values is slightly higher in the wet season. The corrected reflectance of gray objects in the dry season differed by approximately 2.6% (5.6%) when considering the one (two) standard deviation range from the average. The two standard deviation range is only slightly higher than the range of the expected overall algorithm accuracy of $\pm 2.5\%$ [57]. Therefore, we consider it important to derive as precise as possible water vapor loadings for the current state of the atmosphere, but if not available, the use of a climatologic seasonal cycle is a tolerable fallback strategy with a reasonable uncertainty. It might be worth the effort to improve on the water vapor database, e.g., by filling the pre-MODIS era with NOAA-AVHRR-derived water vapor estimates (e.g., [67]), which would, e.g., decrease the risk that inappropriate values would be used in significantly wetter, drier, hotter, or colder years. However, this strategy would necessitate a thorough examination of the different methods and sensors with regard to the continuity of the estimated values and was not yet implemented. In any case, the presence of a clear seasonality in water vapor should be verified for other study areas before using this fallback strategy.

D. Topographic Correction

It was shown that the topographic correction caused a decrease in the correlation strength between $\cos i$ and L in most cases, suggesting that topographic effects are substantially reduced [68]. This effect was more pronounced in the NIR and SWIR bands due to the stronger darkening effect of topographic shadow in the longer wavelength bands [44], where the removal of this effect has a greater impact. On the contrary, the blue band was occasionally affected by an increase in the correlation strength. The blue band is not the best estimator in assessing the topographic effect, because thick haze can completely impede a relationship between $\cos i$ and L . As such, we tend to not overvalue the R^2 increases in the blue band. Random manual investigation points to a successful topographic normalization, which is also supported by the presented example. In addition, it was shown that the implemented topographic correction performed better than the Minnaert fallback option. Cosine-based corrections tend to overcorrect areas under low-illumination conditions [69], and the Minnaert factor's purpose is simply to dampen the correction strength. One way to optimize the Minnaert value would be to estimate it via a linear regression [69] as it is the case for the C-correction. Nevertheless, as

the Minnaert correction is the fallback option in the case that the regression-based C-correction did not work, estimating the Minnaert factor would also not work, and as such, a fixed correction factor is required for this purpose.

VII. OUTLOOK AND CONCLUSION

In a future version of our algorithm, we consider to expand on the radiometric correction module. Further atmospheric gases such as ozone or uniformly mixed gases are to be included, and we also consider to provide a more spatially explicit treatment of AOD by interpolating between the DOs, as done by [13]. Nevertheless, these strategies will only work if there are plenty of DOs, which is a severe constraint in southern Africa [53]. Therefore, the benefit of any further correction should be evaluated with regard to the following: 1) the actual improvement in the corrected reflectance; 2) the extra cost in computing time; 3) the global applicability; and 4) the global data availability that any new add-on would require.

The geometric correction of Landsat L1T data is commonly precise; [19] reported on a global geometric accuracy of ~ 50 m. Nevertheless, southern African L1T data are occasionally poorly coregistered. In our current implementation, we do not account for this potential error source, but an additional bulk-image registration module could be included in the processing chain.

We also intend to prepare and adapt our framework for new Landsat-like systems such as any upcoming Landsat-9+ spacecraft or the soon-to-be-available Sentinel-2 data. We consider our approach to be sufficiently transferable to similar medium-resolution data as we are already processing data from all available Landsat systems with the same algorithm, which is, e.g., not employed in LEDAPS. The gridded data structure, the sensor-specific water vapor absorption coefficients, and the exoatmospheric irradiances will facilitate the incorporation of other data, although specific adaptations will surely be necessary. For Sentinel-2 data, it will be mandatory to include a full BRDF treatment because of the larger swath width. Fortunately, the observing geometry and acquisition frequency of Sentinel-2, combined with Landsat, will also facilitate to obtain BRDF parameters from the data themselves, which is very difficult with Landsat data alone.

As already highlighted by [9], the development of higher level products, from multisensor data, provided in arbitrarily—but regularly—divided tiles is a key component in enabling end users to make the best use of medium-resolution data, both across space and time. Currently, these demands are not fully met. Landsat standard products lack systematic gridding; higher level Sentinel-2 products are currently not planned; and Landsat Legacy, Landsat-8, and Sentinel-2 data are not processed with the same algorithm. As such, we specifically developed our processing strategy to derive gridded surface reflectance and cloud/shadow products from multisensor data—potentially also Sentinel-2 or similar data in the near future. Gridded higher level products will significantly simplify the application of pixel-based algorithms and will also allow a broader range of end users to perform such analyses. We chose sufficiently elaborate methods with as few as possible input

data. As such, we presume that the presented processing framework may even generate consistent and high qualitative data in areas where the general data availability is still low, which we demonstrated for southern Africa. As such, we preferred image-based solutions where applicable, e.g., for aerosol estimation and topographic correction, and opted to not account for BRDF effects until the general applicability to medium-resolution data without any preknowledge of the study area has become more feasible.

ACKNOWLEDGMENT

Landsat and SRTM data courtesy of the USGS. The MODIS data used in this study were acquired as part of the NASA Earth-Sun System Division and archived and distributed by the MODIS Adaptive Processing System. The authors would like to thank all the Principal Investigators and their staff for establishing and maintaining the AERONET sites used in this investigation. KAZA TFCA information and boundary courtesy of Peace Parks Foundation. The authors would also like to thank the two anonymous reviewers whose very constructive comments significantly improved the quality of the final paper.

REFERENCES

- [1] W. B. Cohen and S. N. Goward, "Landsat's role in ecological applications of remote sensing," *BioScience*, vol. 54, no. 6, pp. 535–545, Jun. 2004, doi: 10.1641/0006-3568(2004)054[0535:lrieao]2.0.co;2.
- [2] M. A. Wulder *et al.*, "Landsat continuity: Issues and opportunities for land cover monitoring," *Remote Sens. Environ.*, vol. 112, no. 3, pp. 955–969, Mar. 2008, doi: 10.1016/j.rse.2007.07.004.
- [3] T. Danaher *et al.*, "Remote sensing of tree-grass systems: The Eastern Australian Woodlands," in *Ecosystem Function in Savannas: Measurement and Modeling at Landscape to Global Scales*, M. J. Hill and N. P. Hanan, Eds. Boca Raton, FL, USA: CRC Press, 2010, pp. 175–194, doi: 10.1201/b10275-13.
- [4] C. E. Woodcock *et al.*, "Free access to Landsat imagery," *Science*, vol. 320, no. 5879, p. 1011a, May 2008, doi: 10.1126/science.320.5879.1011a.
- [5] Z. Zhu and C. E. Woodcock, "Object-based cloud and cloud shadow detection in Landsat imagery," *Remote Sens. Environ.*, vol. 118, pp. 83–94, Mar. 2012, doi: 10.1016/j.rse.2011.10.028.
- [6] M. A. Wulder *et al.*, "Opening the archive: How free data has enabled the science and monitoring promise of Landsat," *Remote Sens. Environ.*, vol. 122, no. 0, pp. 2–10, Jul. 2012, doi: 10.1016/j.rse.2012.01.010.
- [7] J. G. Masek *et al.*, "North American forest disturbance mapped from a decadal Landsat record," *Remote Sens. Environ.*, vol. 112, no. 6, pp. 2914–2926, Jun. 2008, doi: 10.1016/j.rse.2008.02.010.
- [8] R. Sonnenschein *et al.*, "Differences in Landsat-based trend analyses in drylands due to the choice of vegetation estimate," *Remote Sens. Environ.*, vol. 115, no. 6, pp. 1408–1420, Jun. 2011, doi: 10.1016/j.rse.2011.01.021.
- [9] M. C. Hansen and T. R. Loveland, "A review of large area monitoring of land cover change using Landsat data," *Remote Sens. Environ.*, vol. 122, no. 0, pp. 66–74, Jul. 2012, doi: 10.1016/j.rse.2011.08.024.
- [10] P. Griffiths *et al.*, "A pixel-based Landsat compositing algorithm for large area land cover mapping," *IEEE J. Sel. Topics Appl. Earth Observ. Remote Sens.*, vol. 6, no. 5, pp. 2088–2101, Oct. 2013, doi: 10.1109/js-tars.2012.2228167.
- [11] D. P. Roy *et al.*, "Web-enabled Landsat Data (WELD): Landsat ETM+ composited mosaics of the conterminous United States," *Remote Sens. Environ.*, vol. 114, no. 1, pp. 35–49, Jan. 2010, doi: 10.1016/j.rse.2009.08.011.
- [12] S. Kobayashi and K. Sanga-Ngoie, "The integrated radiometric correction of optical remote sensing imageries," *Int. J. Remote Sens.*, vol. 29, no. 20, pp. 5957–5985, Oct. 2008, doi: 10.1080/01431160701881889.
- [13] J. G. Masek *et al.*, "A Landsat surface reflectance dataset for North America, 1990–2000," *IEEE Geosci. Remote Sens. Lett.*, vol. 3, no. 1, pp. 68–72, Jan. 2006, doi: 10.1109/lgrs.2005.857030.

- [14] N. Flood *et al.*, "An operational scheme for deriving standardised surface reflectance from Landsat TM/ETM+ and SPOT HRG imagery for Eastern Australia," *Remote Sens.*, vol. 5, no. 1, pp. 83–109, Jan. 2013, doi: 10.3390/rs5010083.
- [15] R. DeFries *et al.*, "Earth observations for estimating greenhouse gas emissions from deforestation in developing countries," *Environ. Sci. Policy*, vol. 10, no. 4, pp. 385–394, Jun. 2007, doi: 10.1016/j.envsci.2007.01.010.
- [16] S. E. Nicholson, "Rainfall and atmospheric circulation during drought periods and wetter years in West Africa," *Monthly Weather Rev.*, vol. 109, no. 10, pp. 2191–2208, Oct. 1981, doi: 10.1175/1520-0493(1981)109<2191:raacdd>2.0.co;2.
- [17] D. M. Olson *et al.*, "Terrestrial ecoregions of the world: A new map of life on earth: A new global map of terrestrial ecoregions provides an innovative tool for conserving biodiversity," *BioScience*, vol. 51, no. 11, pp. 933–938, Nov. 2001, doi: 10.1641/0006-3568(2001)051[0933:teotwa]2.0.co;2.
- [18] R. W. S. Fynn, M. Chase, and A. Röder, "Functional habitat heterogeneity and large herbivore seasonal habitat selection in Northern Botswana," *South African J. Wildlife Res.*, vol. 44, no. 1, pp. 1–15, Apr. 2014, doi: 10.3957/056.044.0103.
- [19] T. R. Loveland and J. L. Dwyer, "Landsat: Building a strong future," *Remote Sens. Environ.*, vol. 122, pp. 22–29, Jul. 2012, doi: 10.1016/j.rse.2011.09.022.
- [20] M. A. Wulder *et al.*, "The global Landsat archive: Status, consolidation, and direction," *Remote Sens. Environ.*, doi: <http://dx.doi.org/10.1016/j.rse.2015.11.032>, to be published.
- [21] "SRTM 1 Arc-Second Global [Web Page]," United States Geol. Survey (USGS), Washington, DC, USA, Sep. 2015. [Online]. Available: <https://lta.cr.usgs.gov/SRTM1Arc>.
- [22] B.-C. Gao and Y. J. Kaufman, "Water vapor retrievals using Moderate Resolution Imaging Spectroradiometer (MODIS) near-infrared channels," *J. Geophys. Res., Atmosp.*, vol. 108, no. D13, pp. ACH4.1–ACH4.10, 2003, doi: 10.1029/2002jd003023.
- [23] Z. Zhu, S. Wang, and C. E. Woodcock, "Improvement and expansion of the Fmask algorithm: Cloud, cloud shadow, and snow detection for Landsats 4–7, 8, and Sentinel 2 images," *Remote Sens. Environ.*, vol. 159, pp. 269–277, Mar. 2015, doi: 10.1016/j.rse.2014.12.014.
- [24] "GDAL—Geospatial Data Abstraction Library," Geospatial Data Abstraction Library (GDAL), Open Source Geospatial Found., Version 1.10.0, 2013. [Online]. Available: <http://www.gdal.org>.
- [25] O. Tange, "GNU parallel—The command-line power tool," *USENIX Mag.*, vol. 36, no. 1, pp. 42–47, 2011.
- [26] D. Frantz *et al.*, "Enhancing the detectability of clouds and their shadows in multitemporal dryland Landsat imagery: Extending Fmask," *IEEE Geosci. Remote Sens. Lett.*, vol. 12, no. 6, pp. 1242–1246, Jun. 2015, doi: 10.1109/lgrs.2015.2390673.
- [27] A. Meijster, J. B. T. M. Roerdink, and W. H. Hesselink, "A general algorithm for computing distance transforms in linear time," in *Mathematical Morphology and Its Applications to Image and Signal Processing*, vol. 18, J. Goutsias *et al.*, Eds. New York, NY, USA: Springer-Verlag, 2000, ch. 36, pp. 331–340.
- [28] D. Tanré *et al.*, "Description of a computer code to simulate the satellite signal in the solar spectrum: The 5S code," *Int. J. Remote Sens.*, vol. 11, no. 4, pp. 659–668, Apr. 1990, doi: 10.1080/01431169008955048.
- [29] P. Teillet, B. Guindon, and D. Goodenough, "On the slope-aspect correction of multispectral scanner data," *Can. J. Remote Sens.*, vol. 8, no. 2, pp. 84–106, Aug. 1982, doi: 10.1080/07038992.1982.10855028.
- [30] J. Hill, "High Precision Land Cover Mapping and Inventory With Multi-Temporal Earth Observation Satellite Data: The Ardèche Experiment," Ph.D. dissertation, Faculty Geogr./Geosci., Trier University, Trier, Germany, 1993.
- [31] D. Tanre, M. Herman, and P. Y. Deschamps, "Influence of the back-ground contribution upon space measurements of ground reflectance," *Appl. Opt.*, vol. 20, no. 20, pp. 3676–3684, Oct. 1981, doi: 10.1364/ao.20.003676.
- [32] G. Chander, B. L. Markham, and D. L. Helder, "Summary of current radiometric calibration coefficients for Landsat MSS, TM, ETM+, and EO-1 ALI sensors," *Remote Sens. Environ.*, vol. 113, no. 5, pp. 893–903, May 2009, doi: 10.1016/j.rse.2009.01.007.
- [33] G. Thuillier *et al.*, "The solar spectral irradiance from 200 to 2400 nm as measured by the SOLSPEC spectrometer from the Atlas and Eureka missions," *Solar Phys.*, vol. 214, no. 1, pp. 1–22, May 2003, doi: 10.1023/a:1024048429145.
- [34] J. Spencer, "Fourier series representation of the position of the sun," *Search*, vol. 2, no. 5, pp. 172–172, May 1971.
- [35] R. E. Bird and C. Riordan, "Simple solar spectral model for direct and diffuse irradiance on horizontal and tilted planes at the earth's surface for cloudless atmospheres," *J. Climate Appl. Meteorol.*, vol. 25, no. 1, pp. 87–97, Jan. 1986, doi: 10.1175/1520-0450(1986)025<0087:sssmfd>2.0.co;2.
- [36] L. Rothman *et al.*, "The HITRAN2012 molecular spectroscopic database," *J. Quantitative Spectroscopy Radiative Transfer*, vol. 130, pp. 4–50, Nov. 2013, doi: 10.1016/j.jqsrt.2013.07.002.
- [37] J. Hill and B. Sturm, "Radiometric correction of multitemporal Thematic Mapper data for use in agricultural land-cover classification and vegetation monitoring," *Int. J. Remote Sens.*, vol. 12, no. 7, pp. 1471–1491, Jul. 1991, doi: 10.1080/01431169108955184.
- [38] H. Gordon, "A preliminary assessment of the Nimbus-7 CZCS atmospheric correction algorithm in a horizontally inhomogeneous atmosphere," in *Oceanography from Space*, vol. 13, J. F. R. Gower, Ed. Boston, MA, USA: Springer-Verlag, 1981, ch. 30, pp. 257–265.
- [39] V. V. Sobolev, "Light scattering in planetary atmospheres," *Translation of Rasseianie sveta v atmosferakh planet, Moscow, Izdatel'stvo Nauka*, 1972, vol. 76, ser. International Series of Monographs in Natural Philosophy. New York, NY, USA: Pergamon, p. 263, 1975.
- [40] W. M. Irvine, "Multiple scattering in planetary atmospheres," *Icarus*, vol. 25, no. 2, pp. 175–204, Jun. 1975, doi: 10.1016/0019-1035(75)90019-6.
- [41] S. Arunachapur, "Satellite remote sensing of atmospheric optical depth spectrum," *Int. J. Remote Sens.*, vol. 7, no. 4, pp. 499–514, Apr. 1986, doi: 10.1080/01431168608954705.
- [42] R. Guzzi, R. Rizzi, and G. Zibordi, "Atmospheric correction of data measured by a flying platform over the sea: Elements of a model and its experimental validation," *Appl. Opt.*, vol. 26, no. 15, pp. 3043–3051, Aug. 1987, doi: 10.1364/ao.26.003043.
- [43] A. Bucholtz, "Rayleigh-scattering calculations for the terrestrial atmosphere," *Appl. Opt.*, vol. 34, no. 15, pp. 2765–2773, May 1995, doi: 10.1364/ao.34.002765.
- [44] Y. Luo, A. P. Trishchenko, and K. V. Khlopenkov, "Developing clear-sky, cloud and cloud shadow mask for producing clear-sky composites at 250-meter spatial resolution for the seven MODIS land bands over Canada and North America," *Remote Sens. Environ.*, vol. 112, no. 12, pp. 4167–4185, Dec. 2008, doi: 10.1016/j.rse.2008.06.010.
- [45] P. S. Chavez, Jr., "An improved dark-object subtraction technique for atmospheric scattering correction of multispectral data," *Remote Sens. Environ.*, vol. 24, no. 3, pp. 459–479, Apr. 1988, doi: 10.1016/0034-4257(88)90019-3.
- [46] A. Royer, L. Charbonneau, and P. M. Teillet, "Interannual Landsat-MSS reflectance variation in an urbanized temperate zone," *Remote Sens. Environ.*, vol. 24, no. 3, pp. 423–446, Apr. 1988, doi: 10.1016/0034-4257(88)90017-X.
- [47] S. Kay, J. Hedley, and S. Lavender, "Sun glint correction of high and low spatial resolution images of aquatic scenes: A review of methods for visible and near-infrared wavelengths," *Remote Sens.*, vol. 1, no. 4, p. 697, Oct. 2009, doi: 10.3390/rs1040697.
- [48] T. F. Eck *et al.*, "Wavelength dependence of the optical depth of biomass burning, urban, and desert dust aerosols," *J. Geophys. Res., Atmosp.*, vol. 104, no. D24, pp. 31333–31349, 1999, doi: 10.1029/1999jd900923.
- [49] A. Ångström, "The parameters of atmospheric turbidity," *Tellus*, vol. 16, no. 1, pp. 64–75, 1964, doi: 10.1111/j.2153-3490.1964.tb00144.x.
- [50] P. Gege, "The water color simulator WASI: An integrating software tool for analysis and simulation of optical in situ spectra," *Computers Geosci.*, vol. 30, no. 5, pp. 523–532, Jun. 2004, doi: 10.1016/j.cageo.2004.03.005.
- [51] S. Jacquemoud *et al.*, "PROSPECT + SAIL models: A review of use for vegetation characterization," *Remote Sens. Environ.*, vol. 113, pp. S56–S66, Sep. 2009, doi: 10.1016/j.rse.2008.01.026.
- [52] D. Frantz *et al.*, "On the derivation of a spatially distributed aerosol climatology for its incorporation in a radiometric Landsat pre-processing framework," *Remote Sens. Lett.*, vol. 6, no. 8, pp. 647–656, Aug. 2015, doi: 10.1080/2150704x.2015.1070314.
- [53] Y. J. Kaufman and C. Sendra, "Algorithm for automatic atmospheric corrections to visible and near-IR satellite imagery," *Int. J. Remote Sens.*, vol. 9, no. 8, pp. 1357–1381, Aug. 1988, doi: 10.1080/01431168808954942.
- [54] S. Hantson and E. Chuvieco, "Evaluation of different topographic correction methods for Landsat imagery," *Int. J. Appl. Earth Observ. Geoinf.*, vol. 13, no. 5, pp. 691–700, Oct. 2011, doi: 10.1016/j.jag.2011.05.001.
- [55] J. A. Smith, "The Lambertian assumption and Landsat data," *Photogramm. Eng. Remote Sens.*, vol. 46, pp. 1183–1189, 1980.

- [56] B. K. P. Horn, "Hill shading and the reflectance map," *Proc. IEEE*, vol. 69, no. 1, pp. 14–47, Jan. 1981, doi: 10.1109/proc.1981.11918.
- [57] A. Röder, T. Kuemmerle, and J. Hill, "Extension of retrospective datasets using multiple sensors. An approach to radiometric intercalibration of Landsat TM and MSS data," *Remote Sens. Environ.*, vol. 95, no. 2, pp. 195–210, Mar. 2005, doi: 10.1016/j.rse.2004.12.008.
- [58] B. N. Holben *et al.*, "AERONET—A federated instrument network and data archive for aerosol characterization," *Remote Sens. Environ.*, vol. 66, no. 1, pp. 1–16, Oct. 1998, doi: 10.1016/S0034-4257(98)00031-5.
- [59] J. R. Nagol *et al.*, "Bidirectional effects in Landsat reflectance estimates: Is there a problem to solve?" *ISPRS J. Photogramm. Remote Sens.*, vol. 103, May 2015, doi: 10.1016/j.isprsjprs.2014.09.006.
- [60] C. B. Schaaf *et al.*, "First operational BRDF, albedo nadir reflectance products from MODIS," *Remote Sens. Environ.*, vol. 83, no. 1/2, pp. 135–148, Nov. 2002, doi: 10.1016/S0034-4257(02)00091-3.
- [61] A. Huete *et al.*, "Overview of the radiometric and biophysical performance of the MODIS vegetation indices," *Remote Sens. Environ.*, vol. 83, no. 1/2, pp. 195–213, Nov. 2002, doi: 10.1016/S0034-4257(02)00096-2.
- [62] D. P. Roy *et al.*, "Multi-temporal MODIS-Landsat data fusion for relative radiometric normalization, gap filling, and prediction of Landsat data," *Remote Sens. Environ.*, vol. 112, no. 6, pp. 3112–3130, Jun. 2008, doi: 10.1016/j.rse.2008.03.009.
- [63] N. Flood, "Continuity of reflectance data between Landsat-7 ETM+ and Landsat-8 OLI, for both top-of-atmosphere and surface reflectance: A study in the Australian landscape," *Remote Sens.*, vol. 6, no. 9, pp. 7952–7970, Aug. 2014, doi: 10.3390/rs6097952.
- [64] S. S. Gillingham *et al.*, "Limitations of the dense dark vegetation method for aerosol retrieval under Australian conditions," *Remote Sens. Lett.*, vol. 3, no. 1, pp. 67–76, Jan. 2011, doi: 10.1080/01431161.2010.533298.
- [65] S. S. Gillingham, N. Flood, and T. K. Gill, "On determining appropriate aerosol optical depth values for atmospheric correction of satellite imagery for biophysical parameter retrieval: Requirements and limitations under Australian conditions," *Int. J. Remote Sens.*, vol. 34, no. 6, pp. 2089–2100, Mar. 2013, doi: 10.1080/01431161.2012.738945.
- [66] T. F. Eck *et al.*, "Characterization of the optical properties of biomass burning aerosols in Zambia during the 1997 ZIBBEE field campaign," *J. Geophys. Res.*, 1984–2012, vol. 106, no. D4, pp. 3425–3448, Feb. 2001, doi: 10.1029/2000JD900555.
- [67] J. A. Sobrino *et al.*, "Atmospheric water vapor content over land surfaces derived from the AVHRR data: Application to the Iberian Peninsula," *IEEE Trans. Geosci. Remote Sens.*, vol. 37, no. 3, pp. 1425–1434, May 1999, doi: 10.1109/36.763306.
- [68] J. Hill, W. Mehl, and V. Radeloff, "Improved forest mapping by combining corrections of atmospheric and topographic effects in Landsat TM imagery," in *Sensors and Environmental Applications of Remote Sensing*, J. Askne, Ed. Rotterdam, The Netherlands: Balkema, 1995, pp. 143–151.
- [69] P. Meyer *et al.*, "Radiometric corrections of topographically induced effects on Landsat TM data in an alpine environment," *ISPRS J. Photogramm. Remote Sens.*, vol. 48, no. 4, pp. 17–28, Aug. 1993, doi: 10.1016/0924-2716(93)90028-L.



David Frantz received the Diploma degree in applied environmental sciences from Trier University, Trier, Germany, in 2012, with a major in remote sensing. He is currently working toward the Ph.D. degree at Trier University.

He is currently a Researcher with the Department of Environmental Remote Sensing and Geoinformatics, Trier University. His research interests cover the monitoring of dryland ecosystems using multispectral optical remote sensing data. His main research focus is on the radiometric mass preprocessing of

remote sensor data, the development and application of data fusion techniques, and the development of pixel-based Landsat compositing algorithms for the monitoring of forest dynamics across large areas.



Achim Röder received the Ph.D. degree in natural sciences from Trier University, Trier, Germany, in 2005, for the development of a remote-sensing-based monitoring framework for Mediterranean rangelands.

He was raised as a geographer. He is currently a Senior Scientist with the Department of Environmental Remote Sensing and Geoinformatics, Trier University. His general scientific interest is on the integration of optical remote sensing and geospatial data analysis for environmental studies. In particular,

he focuses on the assessment of temporal dynamics of land use/cover using change detection and time series analysis techniques and the development of operational spectral mixture analysis concepts. Furthermore, he is interested in analyzing remote-sensing-based change dynamics to identify driving factors and assess tradeoffs in interdisciplinary contexts.



Marion Stellmes received the Diploma degree in applied environmental sciences from Trier University, Trier, Germany in 2002, with an emphasis on optical remote sensing and geomathematics, and the Ph.D. degree from Trier University, Trier, Germany, in 2011.

She is currently a Senior Scientist with the Department of Environmental Remote Sensing and Geoinformatics, Trier University. She is interested in interdisciplinary environmental research, particularly in the evaluation of ecosystem goods and

services, and has a strong background in remote-sensing-based monitoring of land degradation and desertification in the Mediterranean and Southern Africa. Furthermore, she is specialized in time series analysis of medium- and coarse-resolution remote sensing time series and has been working for more than ten years in the field of land cover/use change detection.



Joachim Hill received the Ph.D. degree from Trier University, Trier, Germany, in 1991 and the Postdoctoral degree from Ludwig Maximilians University Munich, Munich, Germany, in 1993.

From 1984 to 1994, he was with the Joint Research Centre of the European Commission in Ispra, Italy. Since 1994, he has been a Full Professor of remote sensing with Trier University, Trier, Germany, where he is also the Head of the Department of Environmental Remote Sensing and Geoinformatics.

He is a member of the scientific advisory group of the Environmental Monitoring and Analysis Program, a German hyperspectral satellite mission to be launched in 2018. His research in remote sensing focuses on data processing strategies for monitoring forest ecosystems and land degradation processes.